JOURNAL OF SOLID STATE CHEMISTRY **131,** 263–274 (1997)
ARTICLE NO. SC977374

The Geometry and Electronic Structure of the Cu^{2+} Polyhedra in Trirutile-Type Compounds $Zn(Mg)_{1-x}Cu_xSb_2O_6$ and the Dimorphism of $CuSb_2O_6$: A Solid State and EPR Study

E.-O. Giere,* A. Brahimi,† H. J. Deiseroth,† and D. Reinen*

*Fachbereich Chemie and Zentrum für Materialforschung, Philipps-Universität Marburg, Marburg, Germany; and †Anorganische Chemie, Universität–GH Siegen, Siegen, Germany

Received October 28, 1996; accepted March 4, 1997

DEDICATED TO PROFESSOR R. BLACHNIK ON THE OCCASION OF HIS 60TH BIRTHDAY

Results from crystal structural analyses of $CuSb_2O_6$ with the trirutile structure, which transforms from the β phase (space group $P2_1/n$) to the α-phase (space group $P4_2/nmn$) at 380 K, are reported. While extensive twinning prevents the single crystal structure determination of the β modification, the α phase reveals compressed CuO_6 polyhedra with Cu–O spacings of 202.6 pm (2×) and 206.6 pm (4×). From the spectroscopic investigation (EPR, optical) of mixed crystals $Zn(Mg)_{1-x}Cu_xSb_2O_6$ with dependence on x and temperature it is deduced that the CuO_6 polyhedra are compressed (spacings $\cong$197 pm (2×) and $\cong$208.5 pm (4×)) for $x < 0.5$ but transform to elongated entities at larger Cu^{2+} concentrations (spacings 200.4 pm (2×), 201.2 pm (2×), and 212.0 pm (2×) from neutron diffraction powder analysis (3)). Evidence for anisotropic π-contributions to the Cu–O bond is presented. A detailed analysis of the ground state potential surface in terms of a vibronic Jahn–Teller coupling model in the presence of a host site strain is given for the two alternative CuO_6 geometries. The Cu–O spacings in α-$CuSb_2O_6$ are explained as resulting from those in the β phase by a dynamic averaging process (201.2 pm (2×), 212.0 pm (2×) → 206.6 pm (4×) above 380 K).

INTRODUCTION

Trirutile-type solids with the chemical composition AB_2X_6 crystallize in the space group $P4_2/mnm$ and two formula units in the unit cell (1, 2) (Fig. 1). Their structure derives from the rutile lattice by tripling the c-axis. As can be deduced from published atomic positions (1) the ZnO_6 octahedra in $ZnSb_2O_6$ are tetragonally compressed along the Zn–O1 bonds in first approximation, with the bond angles in the equatorial plane deviating by $\cong \pm 6^\circ$ from the perpendicular orientation (see Table 3). $CuSb_2O_6$, on the other hand, crystallizes in a monoclinic variant of the trirutile structure (1) and a powder neutron diffraction investigation has been performed (3). The symmetry reduction is due to the Cu^{2+} ion and its tendency to adopt a tetragonally elongated octahedral geometry (4). Indeed in the space group $P2_1/n$ the equivalence of the four equatorial O2 oxygen atoms is lifted (3) so that two of the copper–oxygen bonds become longer while the other two are reduced in length approaching the values of the Cu–O1 spacings (see Table 3). In both structures the MO_6 polyhedra ($M = Zn^{2+}$, Cu^{2+}) possess a center of symmetry.

$CuSb_2O_6$ is reported to exhibit a monoclinic-to-tetragonal phase transition around 500 K (5), in severe contrast to our findings (see below). $Zn(Mg)Sb_2O_6$ and $CuSb_2O_6$ show complete miscibility, with the mixed crystals $Zn_{1-x}Cu_xSb_2O_6$ undergoing a continuous phase transition at 293 K from tetragonal to monoclinic at a critical concentration of $x_c \cong 0.75$ (2). A higher order phase transition is indeed in agreement with group theoretical symmetry relations.

In this study the results of single crystal structure determinations of $CuSb_2O_6$ in the high-temperature α modification and in the low-temperature β modification will be presented. Spectroscopic investigations (EPR, IR, and ligand-field) of the mixed crystal series $Zn(Mg)_{1-x}Cu_xSb_2O_6$ have been performed to elucidate the geometry and the electronic structure of the CuO_6 polyhedra with dependence on x. In particular the interest is focused on the analysis of the transition from the compressed to the elongated octahedral MO_6 coordination, when Zn^{2+} (Mg^{2+}) is successively replaced by Cu^{2+}.

EXPERIMENTAL

Preparation

Although $CuSb_2O_6$ was obtained as the main product with different starting materials (6), the reaction of elemental Cu with Sb_2O_3 under a stream of dry oxygen turned out to be the most effective preparation route. This procedure

0022-4596/97 $25.00

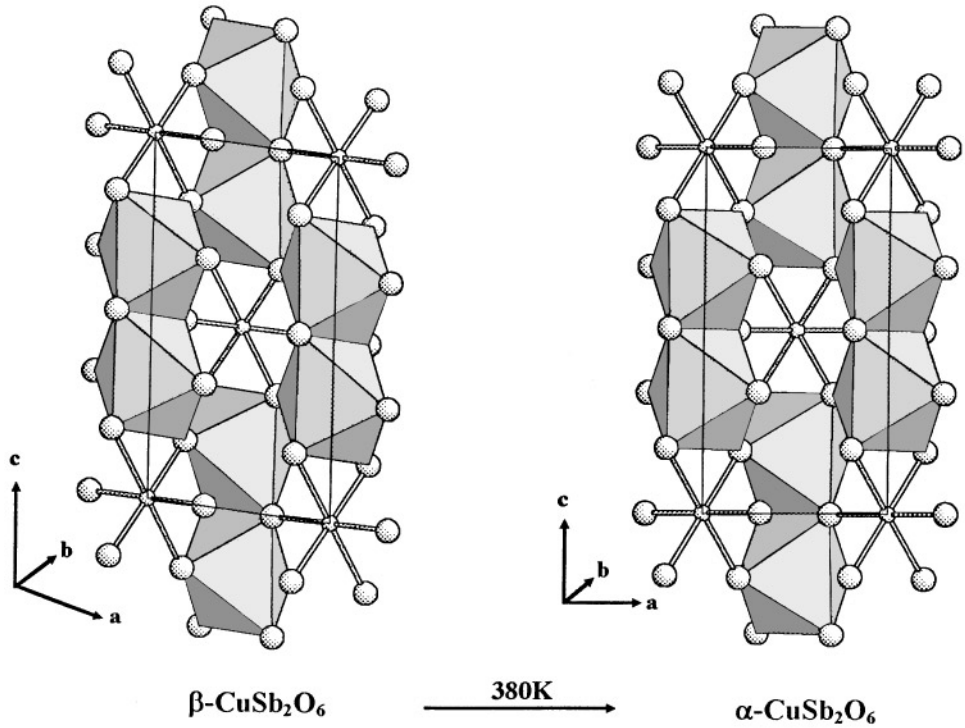

FIG. 1. The tetragonal tritutile unit cell of $ZnSb_2O_6$ and α-$CuSb_2O_6$ (right) compared to the monoclinic cell of β-$CuSb_2O_6$ (left, polyhedron distortion overemphasized); SbO_6 octahedra, shaded; CuO_6/ZnO_6 octahedra, ball and stick.

yields pure $CuSb_2O_6$ by grinding the starting materials Cu and Sb_2O_3, annealing them to 1280 K in a finger-shaped corundum crucible, and exposing them to a continous stream of pure oxygen in a tube of quartz glass. It is important to anneal the starting mixture as fast as possible to avoid vaporization of Sb_2O_3. The microcrystalline reaction product has a light yellow color. Its X-ray diagram, which can be indexed on the basis of the lattice constants published for $CuSb_2O_6$ in (3), does not show any impurities of other phases. It should be mentioned that despite different colors of the $CuSb_2O_6$ samples (black-green to yellow), no significant differences in the X-ray powder diagrams can be detected. Traces of Cu(III) should be responsible for the dark colors due to mixed valence behavior.

Multiply twinned ($T = 293$ K) crystals of β-$CuSb_2O_6$ were obtained from a V_2O_5 flux. The reaction mixture (mass ratio $CuSb_2O_6$: $V_2O_5 \approx 1:4$) was heated to 1170 K in an evacuated quartz ampoule ($l \approx 13$ cm, $\varnothing \approx 12$ mm), kept at this temperature for 24 h, cooled to 970 K, and annealed at this temperature for another 24 h. This procedure yields black, well-shaped β-$CuSb_2O_6$ crystals ($\varnothing \approx 0.1$–0.2 mm), which could be separated microscopically from adhering V_2O_5 and which were suitable for single crystal film investigations. Due to the multiple twinning (see below) originating from the phase transformation with associated symmetry reduction upon cooling, the crystals were unsuitable for diffractometer measurements. When heating those to temperatures above 380 K—a transition temperature distinctly lower than that estimated before (5)—a reversible phase transition to α-$CuSb_2O_6$ takes place without destroying the crystals, now making X-ray single crystal measurements possible (Table 1). Mixed crystals $Zn(Mg)_{1-x}Cu_xSb_2O_6$ were synthesized following the preparation procedure in (2).

TABLE 1
Relevant X-Ray Data for the Single Crystal Measurement of α-$CuSb_2O_6$

Chemical formula	α-$CuSb_2O_6$
Crystal system, space group	Tetragonal, $P4_2/mnm$ (No. 136), $Z = 2$
Lattice constants [pm]	$a = b = 462.91(13)$; $c = 928.82(6)$
X-ray density [Mg/m^3]	6.72
Linear absorption coeff. $\mu_{MoK\alpha}$ [cm^{-1}]	188.3
Diffractometer	SYNTEX $P2_1$, Mo$K\alpha$, ω-scan
Temperature [K]	400
θ range [°]	$2 < 2\theta < 70$
Total number of reflections measured	1620
Number of symmetry independent	265
Symmetry independent with $I > 2.5\sigma(I_0)$	201
Structure refinement	NRCVAX (6)
R values: $R(I > 2.5\sigma(I))$; R(all data)	0.015; 0.021
$wR2$ ($I > 2\sigma(I)$); $wR2$ (all data)	0.016; 0.019

X-ray Investigations of $CuSb_2O_6$ Single Crystals

The multiple twinning of the β-$CuSb_2O_6$ crystals below 380 K, which was carefully analyzed by the precession technique (Mo$K\alpha$), showed up in a specific reflection pattern characterized by a very narrow, fourfold splitting of the BRAGG reflections, which could not be resolved by a corresponding diffractometer measurement. The splitting pattern confirmed the assumed monoclinic symmetry for β-$CuSb_2O_6$, derived from Rietveld refinement of earlier neutron powder data (3) and predicted by a group–subgroup relation described elsewhere (7). Another series of precession photographs of the same crystal, taken well above the transformation temperature of $CuSb_2O_6$ ($T = 380$ K), did not show any reflection splittings and confirmed the ideal tetragonal trirutile structure for α-$CuSb_2O_6$ at temperatures above the transition point. In Table 2 the refined positional and thermal parameters are compared to literature data for β-$CuSb_2O_6$ (3). Table 3 gives important interatomic distances and angles.

RESULTS AND DISCUSSION

The Structure of $CuSb_2O_6$

$CuSb_2O_6$ adopts the ideal tetragonal trirutile structure only in the high-temperature modification ($T > 380$ K). Below 380 K a second-order phase transition from tetragonal α-$CuSb_2O_6$ to monoclinic β-$CuSb_2O_6$ takes place, which inevitably causes a multiple twinning of the respective single crystals. As can be derived from the above mentioned group–subgroup relation (7) and a series of precession photographs of β-$CuSb_2O_6$ crystals, two subsequent symmetry reduction steps, each of index 2, lead to a crystal splitting into four domains. The phase transformation induces a significant splitting of BRAGG reflections on high-resolution powder diagrams. Careful analyses of powder diagrams show the splitting to be basically due to an angular deviation of β from 90° (91.2° at $T = 298$ K) and to a minor extent to different lengths ($\delta \approx 0.2$ pm) of a and b in the monoclinic β modification compared to the tetragonal α modification. It is further interesting to note that the length of the c-axis is nearly temperature independent in the range $298 \leq T \leq 523$ K, whereas $a \cong b$ change significantly with temperature. In contrast to β, which remains 90° for $T > 380$ K, and the unit cell volume V, the temperature dependence of which shows a change in slope around $T = 380$ K, the slope of the temperature dependence of $a \cong b$ does not significantly change at this temperature (Fig. 2).

Concerning the individual CuO_6 and SbO_6 octahedra the phase transition has different consequences. Whereas the average Sb–O spacing shows a slight decrease from 199.3 to 198.3 pm when increasing the temperature from 293 to 400 K, the average Cu–O distance increases slightly from 204.5 to 205.6 pm. In particular, one deduces (Fig. 3) that the CuO_6 octahedron switches from an *elongated* form (α-$CuSb_2O_6$) to a *compressed* form, with the directions of elongation and compression not being the same (Table 3). In the low-temperature modification the direction of elongation is along the O2a–Cu bonds (212.0 pm), with Cu–O2 and Cu–O1 spacings of 201.2 (2×) and 200.4 pm (2×), respectively, in the equatorial plane. In the high-temperature form, however, the Cu–O1 bonds (202.6 pm) mark the direction of compression, with longer Cu–O2 distances of 206.6 pm (4×) in the plane perpendicular to this direction.

TABLE 2

Comparison of the Positional and Isotropic Thermal Displacement Parameters (Standard Deviations in Parentheses) for α-$CuSb_2O_6$ (First Row, $T = 400$ K, Space Group $P4_2/mnm$, This Work) and β-$CuSb_2O_6$ (Second (and Third) Row, Taken from (3), Space Group $P2_1/n$)

Atom	Position	x	y	z	B[Å]
Cu	2*a*	0	0	0	0.64(9)
	2*a*	0	0	0	
Sb	4*e*	0	0	0.33249(3)	0.47(2)
	4*e*	0.0011(9)	0.008(1)	0.3338(6)	
O1	4*f*	0.3095(8)	0.3095(8)	0	0.61(9)
	4*e*	0.3130(9)	0.2983(8)	0.00174(4)	
O2	8*j*	0.3014(5)	0.3014(5)	0.3271(3)	0.74(6)
	4*e*	0.2991(8)	0.3176(7)	0.3291(4)	
	4*e*	− 0.3012(8)	− 0.2915(9)	0.3248(4)	

TABLE 3

Comparison of Important Interatomic Distances (pm) and Angles (°) for $ZnSb_2O_6$ (Taken from (1), No Standard Deviations Given), β-$CuSb_2O_6$ (Taken from (3)), and α-$CuSb_2O_6$ (This Work), with Standard Deviations in Parentheses

$ZnSb_2O_6$	β-$CuSb_2O_6$	α-$CuSb_2O_6$
	Distances	
Zn–O1: 202 2×	Cu–O1: 200.4(4) 2×	Cu–O1: 202.6(5) 2×
–O2: 205 4×	–O2: 201.2(4) 2×	–O2: 206.6(2) 4×
	–O2a: 212.0(4) 2×	
Sb–O1: 200 2×	Sb–O1: 199.4(6), 201.3(7)	Sb–O1: 199.4(3) 2×
–O2: 200 2×	–O2: 199.3(6), 199.6(6)	–O2: 197.4(3) 2×
197 2×	–O2a: 196.0(6), 197.3(6)	197.1(2) 2×
	Angles	
O1–Zn–O2: 90 8×	O1–Cu–O2: 87.2(2) 2×	O1–Cu–O2: 90 8×
O2–Zn–O2: 78.5 2×	92.3(2) 2×	O2–Cu–O2: 78.0(2) 2×
101.5 2×	O1–Cu–O2a: 90.3(2) 2×	102.0 (2) 2×
	89.7(2) 2×	
	O2–Cu–O2a: 77.7(2) 2×	
	102.3(2) 2×	
O1–Sb–O1: 79.3	O1–Sb–O1: 79.1(3)	O1–Sb–O1: 77.4(2)
O1–Sb–O2: 91.0 4×	O1–Sb–O2: 94.5(3);	O1–Sb–O2: 91.14(3) 4×
99.3 2×	99.6(3); 90.4(3)	100.0(1) 2×
O2–Sb–O2: 82.2	O1–Sb–O2a: 89.2(3);	O2–Sb–O2: 82.5(1)
89.0 4×	91.7(3); 99.5(3)	88.91(2) 4×
	O2–Sb–O2: 88.3(2)	
	O2–Sb–O2a: 87.7(3);	
	89.8(3); 81.9(3);	
	O2a–Sb–O2a: 88.7(2)	

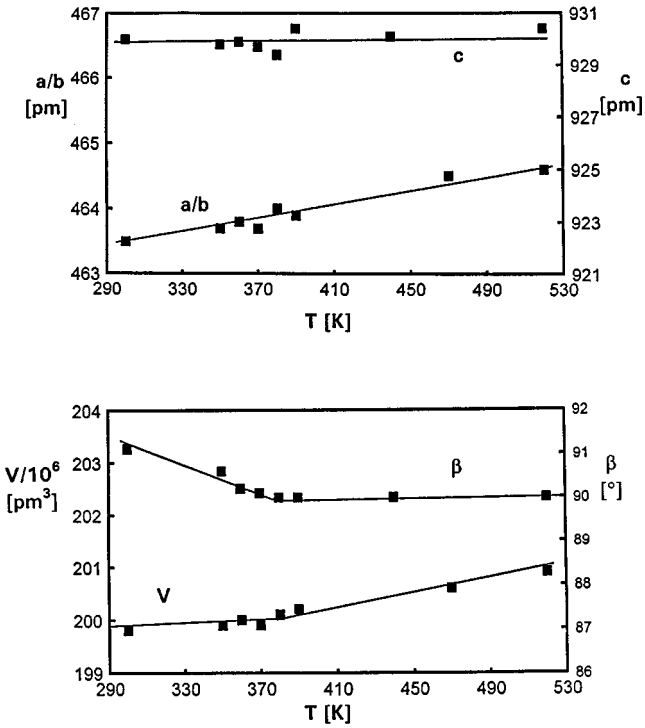

FIG. 2. The thermal expansion of the lattice parameters and the unit cell volume for $CuSb_2O_6$in the temperature range $298 < T < 523$ K (errors correspond to the size of the symbols).

In contrast, the Sb–O distances change only slightly when passing the phase transition. Whereas they lie in the range from 196.0 to 201.3 pm in β-$CuSb_2O_6$, this range is between 197.1 and 199.4 pm in α-$CuSb_2O_6$. The largest angular deviation from 90° is found along the direction of edge sharing of CuO_6 and SbO_6 octahedra. Whereas the angle O2a–Cu–O2 is 77.7° for β-$CuSb_2O_6$, the corresponding value is 78.0° for α-$CuSb_2O_6$ (Fig. 3).

IR and Raman Spectra of $CuSb_2O_6$

Earlier observations of temperature-dependent changes in the IR and Raman spectra (8, 9) of $CuSb_2O_6$ could not be interpreted unambigously, because the phase transition and associated structural details were not known. According to the lattice dynamical calculations of Husson *et al.* (9) the differences in both types of spectra are not due to vibrations of the CuO_6 octahedra but mainly originate from vibrations of the Sb_2O_{10} units. By analogy with results obtained for $MgTa_2O_6$ (9) we assign the IR band of α-$CuSb_2O_6$ observed at 700 cm^{-1}, as well as the Raman line at 645 cm^{-1}, to vibrations of the O2 atoms, which link the Sb_2O_{10} unit to the CuO_6 octahedra (Fig. 4).

According to Husson *et al.* (9) these vibrations belong to the degenerate species E_u and E_g, respectively. By symmetry reduction in the low-temperature form the degeneracy is

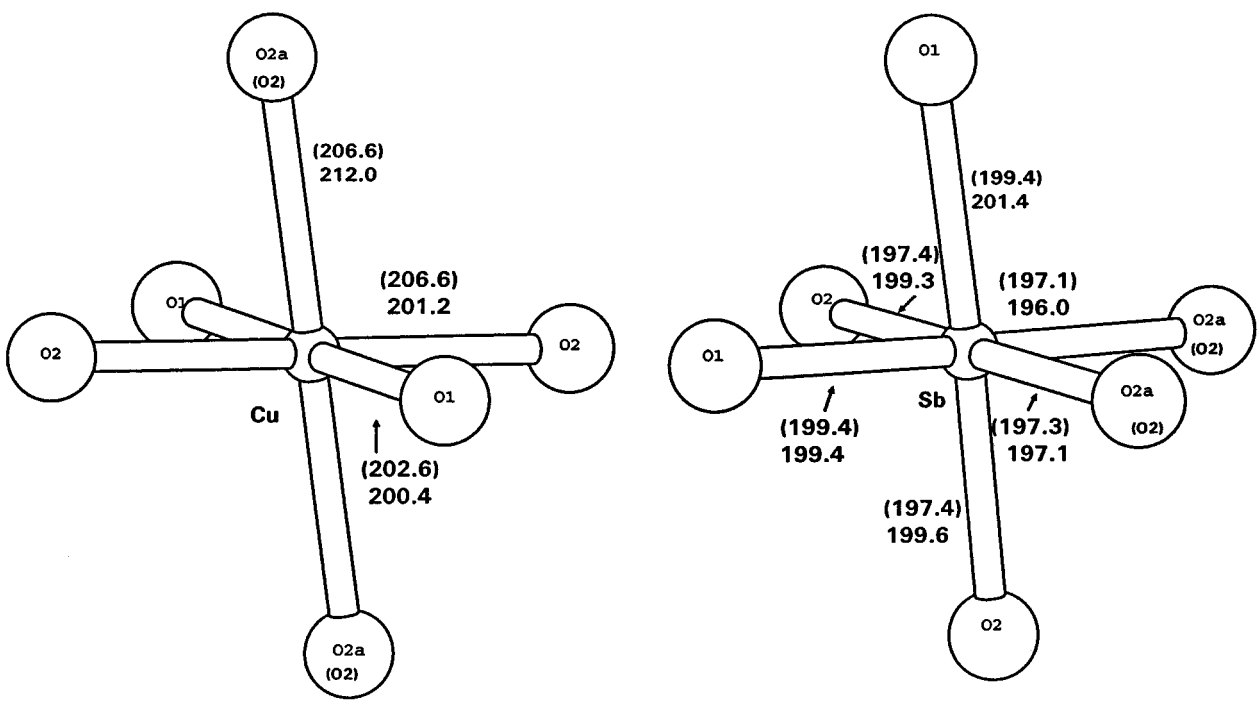

FIG. 3. Interatomic distances (pm) for the CuO_6 and SbO_6 octahedra in α- (in parentheses)and β-$CuSb_2O_6$.

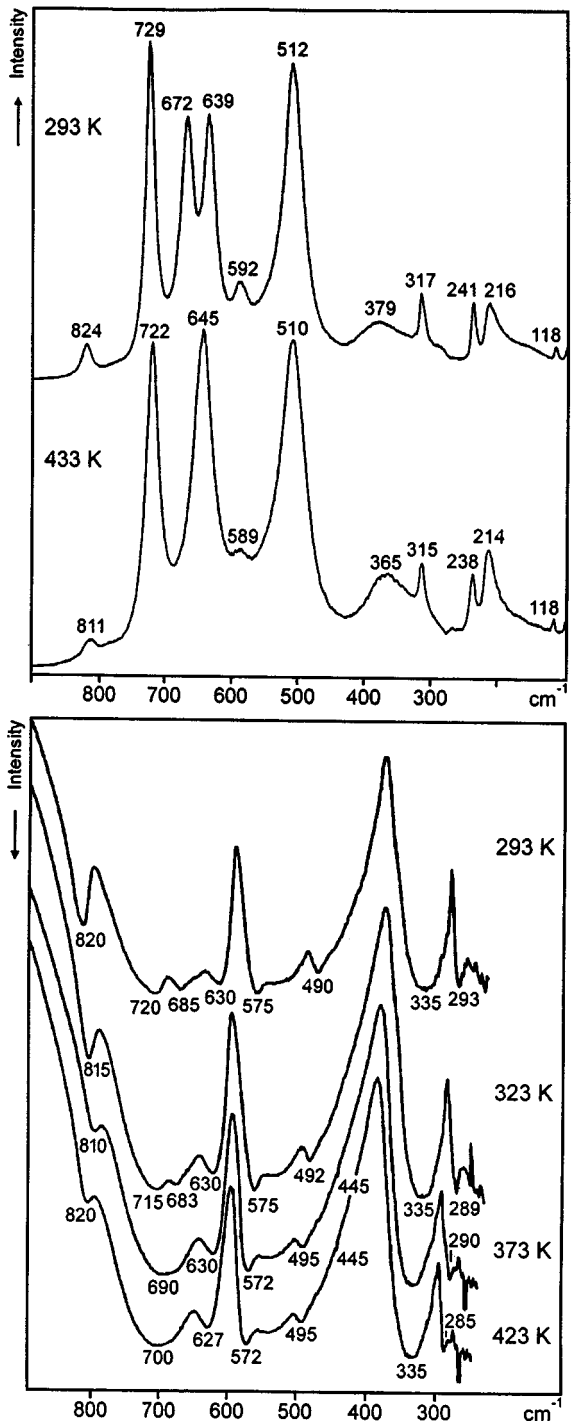

FIG. 4. Temperature dependent IR (bottom) and Raman spectra (top) of $CuSb_2O_6$.

lifted. It is interesting to note that the intensities of the Raman lines at 639 and 672 cm^{-1} are nearly half of that at 645 cm^{-1}, thus confirming the interpretation of being generated by a splitting of the E_g mode.

EPR analysis of Mixed Crystals $Zn_{1-x}Cu_xSb_2O_6$

Figure 5 shows the X-band EPR spectrum of Cu^{2+}-doped $ZnSb_2O_6$($x = 0.01$) at 4 K. It exhibits the typical features expected for a tetragonally compressed CuO_6 octahedron with resolved hyperfine structures induced by the electron–nucleus interaction of copper. The g values and hyperfine splitting constants A are collected in Table 4. At Q-band frequencies a small orthorhombic splitting of the $g_\perp$ signal ($\delta_g \cong 0.01_5$) is resolved, which is not seen in the X-band spectra. Apparently Cu^{2+} adopts the host site ZnO_6 symmetry, even with the expected small lower symmetry distortion component due to the angular distortion in the equatorial plane (Table 3). There is no significant temperature dependence of the g values observed.

Equation [1] gives expressions for g and A relevant for an $^2A_{1g}$ (d_z^2) ground state of Cu^{2+} in a compressed D_{4h} coordination (10),

$$g_\parallel = g_0 \qquad u_{\parallel(\perp)} = k_{\parallel(\perp)}^2\, \zeta_0/E[A_1 \rightarrow B_2(E)]$$
$$g_\perp = g_0 + 6u_\perp$$

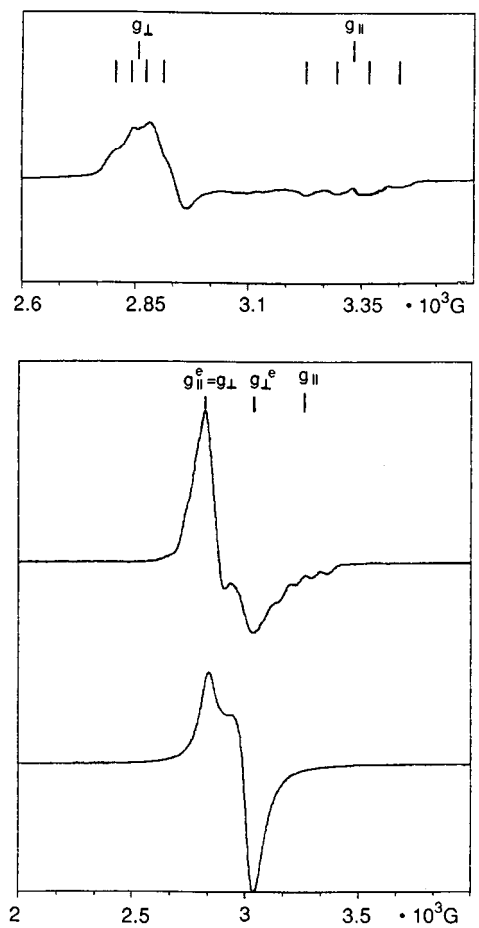

FIG. 5. X-band EPR spectra (4 K) of mixed crystals $Zn_{1-x}Cu_xSb_2O_6$ with $x = 0.01$, 0.10, 0.25 (from above).

TABLE 4
EPR Parameters for Mixed Crystals $Zn_{1-x}Cu_xSb_2O_6$ ($g^{e'}$-Tensor Components Refer to Compounds with $x \geq 0.5$)

x	$T(K)$	$g_\parallel$	$g_\perp$		g_{av}
0.01[a]	4	2.02_1	$\cong 2.35$	X	$\cong 2.24$
0.1[b]	4	2.01_7	2.33_5	X	2.23
	25	2.02_5	2.34_2^c	Q	2.23_5
		$g_1^{e'}$	$g_2^{e'}$ $g_3^{e'}$		g_{av}
0.5	4	$\cong 2.13$	$\cong 2.19$ $\cong 2.35$	Q	$\cong 2.22_5$
0.75	4	2.11_1	2.19_5 2.36_2	X, Q^d	2.22_5
	100	2.11_5	$\cong 2.21$ $\cong 2.35_5$	Q	2.22_5
1.0	25	$\cong 2.10$	$\cong 2.20$ $\cong 2.35$	Q	$\cong 2.22$

[a] Hyperfine splittings: $|A_z| \cong 67 \times 10^{-4}\,cm^{-1}$, $|A_{xy}| \cong 40 \times 10^{-4}\,cm^{-1}$. To obtain meaningful bonding arguments, parameters A_z and A_{xy} have to be chosen positive and negative, respectively.

[b] Additional signal of exchange origin at $g_\perp^e \approx 2.17$ (see text).

[c] Splitted into two signals at 2.33_5 and 2.35 (see text).

[d] The EPR parameters of the simulated spectrum are given in legend for Fig. 6.

$$A_\parallel = P[-\alpha^2(\kappa - 4/7) - 1/7(g_\perp - g_0)]$$
$$A_\perp = P[-\alpha^2(\kappa + 2/7) + 15/14(g_\perp - g_0)]$$
$$\Psi_g = \alpha d_z^2 - \alpha' L_z^2,$$

where ζ_0, k, and E are the free-ion spin–orbit coupling constant of Cu^{2+} ($830\,cm^{-1}$), the covalency parameter, and specific d–d transitions (see below), respectively. The Fermi contact term κ and the calibrating constants P have the values 0.43 and $360 \times 10^{-4}\,cm^{-1}$ for the free Cu^{2+} ion. α is the mixing coefficient in the ground state MO, where L_z^2 represents the symmetry adapted linear combination of ligand orbitals. In contrast to Eq. [1], $g_\parallel$ has a value slightly larger than $g_0 = 2.0023$. This feature can be traced back to a $d_{x^2-y^2}$ contribution to the ground state wavefunction and will be commented on later. From the orbital contribution $u_\perp \cong 0.056$ and the relevant ligand field transition (see next section) a covalency parameter $k_\perp \approx 0.82_5(2)$ is estimated. The calculated α value is 0.91, while the decrease in $\kappa \cong 0.29$ with respect to 0.43 indicates significant contributions from $4s$ in the ground state (10). This is expected because d_z^2 and s possess the same a_{1g} symmetry already in D_{4h} symmetry. The correlation of the g values with the chosen molecular coordinate system is given in Fig. 9.

If the Cu^{2+} concentration is raised above $x \cong 0.1$ a new perpendicular signal around 2.17 ($g_{23}^e = g_\perp^e$) appears, while the $g_\parallel$ signal looses intensity (Fig. 5). The former signal becomes more prominent with increasing x, while the latter soon vanishes. This observation can be explained by exchange interactions between Cu^{2+} centers, which occupy both magnetically inequivalent M^{2+} positions in the unit cell. The $g_\parallel$ values of the two tetragonal centers, which are correlated with the short Cu–O1 directions (Table 3), form a canting angle of $2\gamma = 90°$ with each other, leading to an exchange-coupled g^e tensor with the components given in

$$g_2^e = \sin^2\gamma\, g_\parallel + \cos^2\gamma\, g_\perp, \quad g_3^e = \cos^2\gamma\, g_\parallel + \sin^2\gamma\, g_\perp,$$
$$g_1^e = g_\perp; \quad \cos 2\gamma = g_2^e - g_3^e/g_2^e + g_3^e - 2g_1^e \qquad [2]$$
$$\gamma = 45°: \quad g_1^e = g_\perp, \quad g_{23}^e = g_\perp^e = 1/2(g_\parallel + g_\perp).$$

$g_\perp^e$ is calculated appear at 2.18, near the position of observation (Table 4, Fig. 5). Though the two Cu^{2+} centers lie isolated in the trirutile lattice with Cu–Cu spacings of 5.3 Å (Fig. 3), an exchange integral according to $|J|/k \approx 1\,cm^{-1}$ will already suffice for averaging the g tensor components (Eq. [2]).

A drastic change of the EPR spectrum occurs at $x \cong 0.5$. The exchange-averaged spectrum resulting from the two compressed magnetically inequivalent Cu^{2+} polyhedra is replaced by a new orthorhombic spectrum (Fig. 6, Table 4). At Q-band frequencies the g anisotropy is resolved sufficiently well. As will be outlined in detail below, a consistent

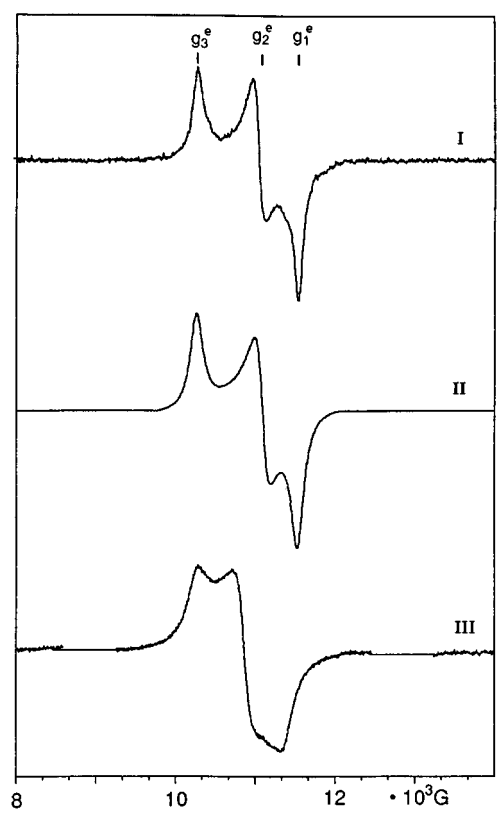

FIG. 6. Q-band EPR spectra of mixed crystals $Zn_{1-x}Cu_xSb_2O_6$ with $x = 0.75$ at 10 K (I), 1.0 at 75 K (III). For $x = 0.75$ the simulated spectrum (chosen parameters: $\Delta H = 57.5$ G; $A = 5 \times 10^{-4}\,cm^{-1}$; $g_1^{e'} = 2.110$, $g_2^{e'} = 2.193$, $g_3^{e'} = 2.369$) is also shown (II).

assignment is only possible with the assumption of a local tetragonally elongated coordination geometry—as occurring in β-$CuSb_2O_6$—and again assuming exchange interactions.

Figure 9 depicts the chosen molecular coordinate system and its correlation with the bond lengths and g tensor components for the cases of the compressed and elongated CuO_6 polyhedron. An elongated D_{4h} coordination (along x, see Fig. 9) of Cu^{2+} implies a $^2B_{1g}$ ($d_{y^2-z^2}$) ground state and would induce the g and A tensor components (10) listed in

$$g'_{\parallel} = g_0 + 8u'_{\parallel} \qquad u_{\parallel(\perp)}' = k_{\parallel(\perp)}{}'^2\,\zeta_0/E[B_{1g} \rightarrow B_{2g}(E_g)]$$
$$g'_{\perp} = g_0 + 2\,u'_{\perp}$$
$$A'_{\parallel} = P[-\alpha^2(\kappa' + 4/7) + 3/7(g'_{\perp} - g_0) + g'_{\parallel} - g_0]$$
$$A'_{\perp} = P[-\alpha^2(\kappa' - 2/7) + 11/14(g'_{\perp} - g_0)]$$
$$\Psi_g = \alpha\, d_{y^2-z^2} - \alpha' L_{y^2-z^2}. \qquad [3]$$

Here, the mixing coefficient α refers to the $d_{y^2-z^2}$ orbital rather than being correlated with d_z^2 as in Eq. [1]. Equation [3] implies—in agreement with experimental experience and symmetry arguments—that the equatorial plane of the short Cu–O1(2) spacings (neglecting the small orthorhombic component) correlates with $g'_{\perp}$, while $g'_{\parallel}$ has the direction of the normal to this plane rather than that of the long Cu–O2a bond, which forms an angle of about 12° with this normal (see the structural data for β-$CuSb_2O_6$ in Table 3).

The three observed exchange-coupled $g^{e'}$ tensor components (Table 4: $g_1^{e'} = 2.11$, $g_2^{e'} = 2.19_5$, $g_3^{e'} = 2.37$) are expected to be oriented parallel and perpendicular to the b unique axis of the monoclinic β-$CuSb_2O_6$ unit cell, which—though not yet apparent in the lattice metric—is already symmetry determining at higher Cu^{2+} concentrations. The structural angle 2γ between the just defined normal directions of the two magnetically inequivalent CuO_6 polyhedra in β-$CuSb_2O_6$ is 52° and located in the ac plane. Utilizing Eq. [2], which is equally valid for local compressed and elongated D_{4h} geometries, in a slightly modified form one obtains the molecular g values in

$$g_z = 2.11, \quad g_y \cong 2.13_5; \quad g_x \cong 2.43;$$
$$k'(d_{xz}, d_{yz}) \approx 0.82(3), \quad k'(d_{xy}) \cong 0.89. \qquad [4]$$

Because the $g^{e'}$ tensor components do not vary with the Cu^{2+} concentration in the range $0.5 \leq x \leq 1.0$ it is indeed expected that the structural angle for β-$CuSb_2O_6$ should reproduce the EPR results. The covalency factors derived from Eq. [3], modified with respect to orthorhombic symmetry and based on the calculated d–d band positions (see below), are those in Eq. [4]. As will be discussed in the next section in detail, the strongly diverging k values are caused by a π (anti)bonding anisotropy of considerable magnitude. While $k'(d_{xz}, d_{yz})$ equals the $k_{\perp}$ parameter for the compressed octahedron ($0.82_5(2)$), the component $k'(d_{xy})$ is considerably larger, indicating strongly reduced π bonding.

Magnetic susceptibility data between 10 and 350 K indicate that β-$CuSb_2O_6$ is a linear chain Heisenberg antiferromagnet with $J/k = -47$ K (3, 11). Three-dimensional ordering seems to occur at $T_c = -8.5$ K, the interchain coupling being of rather complex nature, however (11). From temperature-dependent EPR measurements, one deduces that the signal linewidth strongly decreases when the temperature is lowered, reaching its final value at about 190 K. The signal intensity also decreases with decreasing temperature, the spectrum still persisting down to 5 K (as in the case of the mixed crystals with $x < 1.0$). The latter result is not in contradiction to the magnetic structure below 8.5 K, which is presumably of frustrated nature (11).

The analysis of the low-temperature EPR spectra yields that tetragonally compressed CuO_6 polyhedra are present at Cu^{2+} concentrations $x < 0.5$ while above this critical concentration the distortion geometry switches to a tetragonal elongation, which is characteristic for β-$CuSb_2O_6$ (Table 3). There are even indications that in a narrow concentration range around $x \approx 0.5$ both types of clusters are present side by side. The radial distortion parameter ρ,

$$\rho = \{2(\delta a_x^2 + \delta a_y^2 + \delta a_z^2)\}^{1/2} \qquad [5]$$

where the δa_i ($i = x, y, z$) are the deviations of the Cu–O bond lengths from the averaged spacing, is calculated to be $\cong 13$ pm for the CuO_6 polyhedra in β-$CuSb_2O_6$. It is rather small in comparison to other host lattices and hints toward an unusually stiff polyhedron-connection pattern. The presumable reason is the Sb(V) octahedra in the environment of the divalent cations, giving the CuO_6 polyhedron not much geometrical freedom for a more distinct Jahn–Teller distortion.

In the concentration region of compressed CuO_6 octahedra magnetic short-range interactions between magnetically inequivalent polyhedra occur, which are of the antiferrodistortive kind (canting angle $2\gamma = 90°$) (4, 12). Above $x > 0.5$ the elongated octahedra are equally magnetically correlated, but with a canting angle around 65°, suggesting that, for β-$CuSb_2O_6$, below the short-range-to-long-range transition at 8.5 K a ferromagnetic component might be present.

It may be interesting to compare the above EPR results with those for the $Mg_{1-x}Cu_xSb_2O_6$ mixed crystal series. Similar spectra are observed, but with some distinctions compared to the Zn^{2+} solid solution. On one hand, the g values of the isolated compressed CuO_6 octahedra at very low doping concentrations ($g_{\parallel} = 2.01_0$; $g_{\perp} \cong 2.32$, $g_{\perp}^{e} \cong 2.16_5 - g_{av} \cong 2.22$) are indicative of a more pronounced host-site compression, because the deviation of $g_{\parallel}$ from g_0 is comparatively smaller (see the discussion below). On the

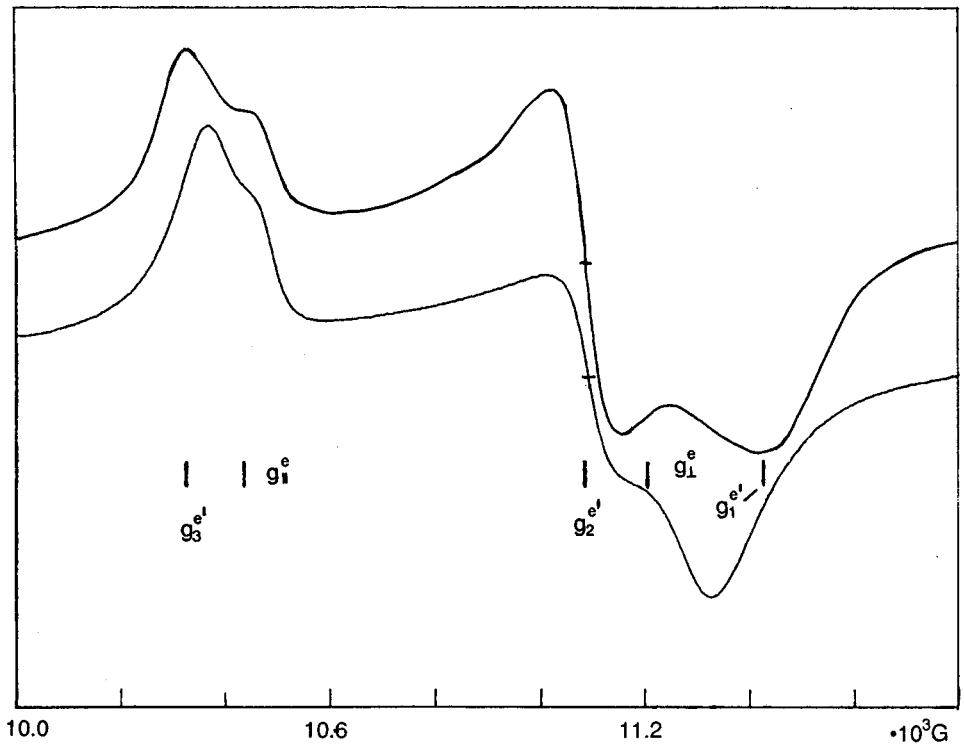

FIG. 7. Q-band EPR spectra of $Mg_{1-x}Cu_xSb_2O_6$ mixed crystals with $x = 0.5$ (16 K, below) and 0.9 (4 K, above). Exchange-coupled clusters of compressed ($g^e_\parallel$, $g^e_\perp$) and elongated CuO_6 octahedra ($g^{e'}_1$, $g^{e'}_2$, $g^{e'}_3$) are seen. See text for numerical values.

other hand, the concentration range, where clusters of exchange-coupled compressed and elongated CuO_6 octahedra ($g^{e'}_3 = 2.35$; $g^{e'}_2 = 2.19$; $g^{e'}_1 = 2.12 - g_{av} \cong 2.22$, nearly identical to the $g^{e'}$ tensor components in Table 4) coexist, extends to higher x values (Fig. 7). While at lower Cu^{2+} concentrations the spectra overlap with nearly equal intensities ($x = 0.5$, Fig. 7), the signals connected with the elongated octahedron dominate in intensity at high x values ($x = 0.9$).

d–d Transitions

Additional information about the extent of the CuO_6 polyhedron distortion and the Cu–O bond properties is provided by the optical spectra in the region of the *d–d* transitions (Fig. 8). They are characterized by a broad band with a maximum at 11,400 cm^{-1} and a shoulder around 9000 cm^{-1}. The resolution is not improved when the temperature is decreased to 5 K. Surprisingly at the first sight no changes in the band positions and in the intensity distribution are observed when switching from the compressed to the elongated coordination geometry. However, this feature is readily explained by looking at those orbitals of the oxygen atoms in the trirutile structure (Fig. 1) which are used for π overlap with the copper d_{xy}, d_{xz}, and d_{yz} orbitals. Because each oxygen atom possesses an approximately trigonal-planar cationic coordination corresponding to a sp^2 hybridization, only one orbital perpendicular to this plane can be used for π bonding (Figs. 9a and 9b). This introduces a π anisotropy into the Cu–O bonding in the tetragonal trirutile structure, which would be even present in the case of equal bond lengths, reducing the local CuO_6 symmetry from O_h to D_{2h}. Neglecting the deviations ($\pm 6°$) of the bond angles from 90° in the equatorial plane, the *d* contributions to the metal–oxygen bonding can be nicely parametrized within the frame of the "angular-overlap model" (AOM). In this model parameters e_σ and e_π describe the σ- and π-antibonding energies of the *d* orbitals in the respective point group (13). Figure 9c depicts the corresponding *d*-orbital energy diagram, showing that a distinct splitting of the t_{2g} levels occurs by the described π effect even in a formal O_h geometry.[1]

[1]While the d_{xy} orbital is nonbonding, the AOM determinant for the d_{xz} and d_{yz} orbitals is

$$\begin{vmatrix} 2e^x_\pi + e^z_\pi - E & e^z_\pi \\ e^z_\pi & 2e^y_\pi + e^z_\pi - E \end{vmatrix} = 0,$$

the indices x, y, z referring to the oxygen p orbital with π-bonding ability in the respective molecular direction (see Fig. 9b). In the case of equal Cu–O bond lengths in the xy plane, the solutions are $2e^{xy}_\pi$ with a $1/\sqrt{2}\,(d_{xz} - d_{yz})$ and $2(e^{xy}_\pi + e^z_\pi)$ with a $1/\sqrt{2}\,(d_{xz} + d_{yz})$ eigenfunction (Fig. 9c).

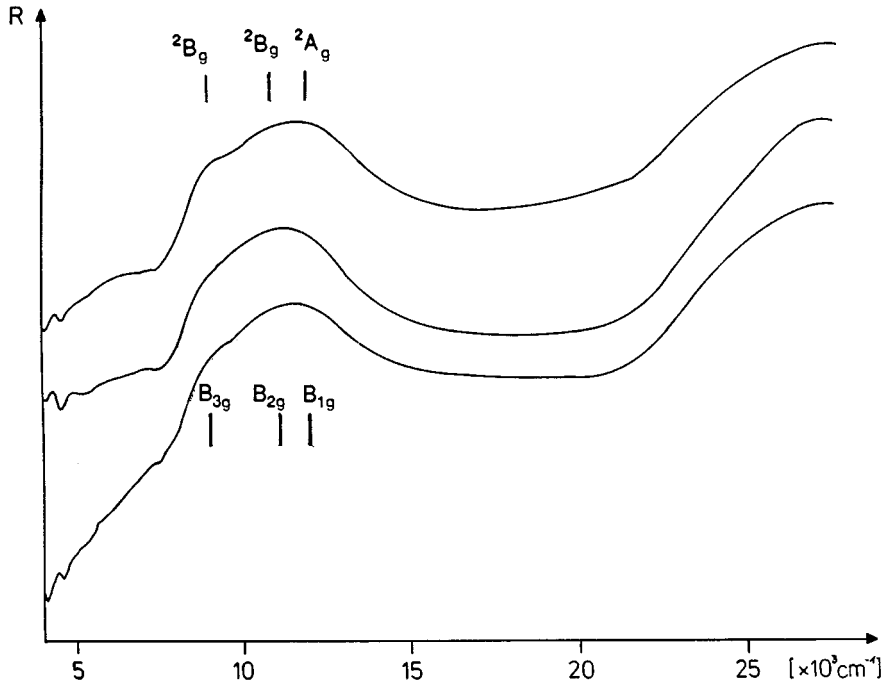

FIG. 8. Ligand field reflection spectra of mixed crystals $Zn_{1-x}Cu_xSb_2O_6$ with $x = 0.3$, 0.5, and, 1.0, from below (298 K; intensity scale, reflectivity R in arbitrary units). For the band assignment (calculated d–d transition energies for the compressed—D_{2h}, below—and the elongated octahedron—C_{2h}, above—are indicated) see Fig. 10. The weak absorptions below 8000 cm^{-1} are due to H_2O or OH^- overtones.

An additional tetragonal compression along the Cu–O1 bond or elongation along the Cu–O2a bond direction, the latter distortion reducing the symmetry to C_{2h} (Fig. 9b), will split the σ-antibonding e_g level. The corresponding $^2A_{1g} \rightarrow {}^2B_{1g}$ or $^2B_{1g} \rightarrow {}^2A_{1g}$ transition (D_{4h} labeling) should occur below 4000 cm^{-1}, the limit of the accessible spectra region, however, because the CuO_6 polyhedron distortion is small ($\rho \cong 0.13$ Å); see Figs. 9c and 10. Indeed the d–d spectra are empty below 9000 cm^{-1} (Fig. 8).[2] The transition from the compressed to the elongated octahedron does not affect the AOM energies much, as can be deduced from Fig. 10, if the same radial distortion parameter is chosen for both geometries (this point will be discussed below). The energy sequence of the split states of the octahedral $^2T_{2g}$ term is mainly determined by the π anisotropy depicted in Fig. 9b. The splittings due to Cu–O distance variations are less important. The chosen AOM parameter set nicely reproduces the d–d band positions (Fig. 10). While the averaged $^2A_g \rightarrow {}^2B_{1g}$, $^2B_{2g}$ (^2A_g, ^2B_g) transition energy is calculated to occur at 11500 cm^{-1}, the $^2A_g \rightarrow {}^2B_{3g}$ (^2B_g) absorption is expected at 9000 cm^{-1}. The splitting of the octahedral ^2E_g ground state is estimated to be of the magnitude 2150 cm^{-1}.

[2]The band maximum at ≈ 4000 cm^{-1} in (2) assigned to this transition seems to be an artifact, caused by the specific absorption properties of the SbO_6 polyhedra. To exclude this effect we have used here the host compound $ZnSb_2O_6$ as the white standard.

We may at this stage conclude that the concentration independence of the ligand field spectra has two reasons. First, the discussed π-bonding anisotropy does not significantly depend on the direction of the distortion of the CuO_6 octahedron, so long as the bond length changes are not too large in magnitude. Second, the extent of the distortion, as measured by the radial distortion parameter ρ, remains constant for all x values. The latter condition implies Cu–O spacings in the compressed octahedron below $x = 0.5$ of $a_z \cong 197$ pm (2×), $a_{xy} \cong 208.5$ pm (4×), calculated from Eq. [5] with the same average bond length $a = 204.5$ pm as for the elongated CuO_6 polyhedron in β-$CuSb_2O_6$ (Table 1).

With the AOM parameters $e_\alpha = 3675$ cm^{-1} and $e_\pi = 720$ cm^{-1} for a regular octahedron with spacings of 204.5 pm and the discussed π-bonding restrictions in the trirutile structure, the term diagrams in Fig. 10 result. Here the e_σ and e_π values for the spacings characterizing the compressed and the elongated octahedron, respectively, have been estimated by using the relationship

$$e_i^j = (S_i^{j2}/S_i^2)e_i \quad (i = \sigma, \pi; j = x, y, z), \qquad [6]$$

where the S_i^j, S_i are tabulated overlap integrals for the Cu–O bond (14). Here e_i (S_i) and the e_i^j (S_i^j)'s refer to the Cu–O bond lengths in the regular octahedron and in the distorted octahedra, respectively. The chosen parameter set corresponds to an octahedral ligand field parameter of $\Delta \cong$

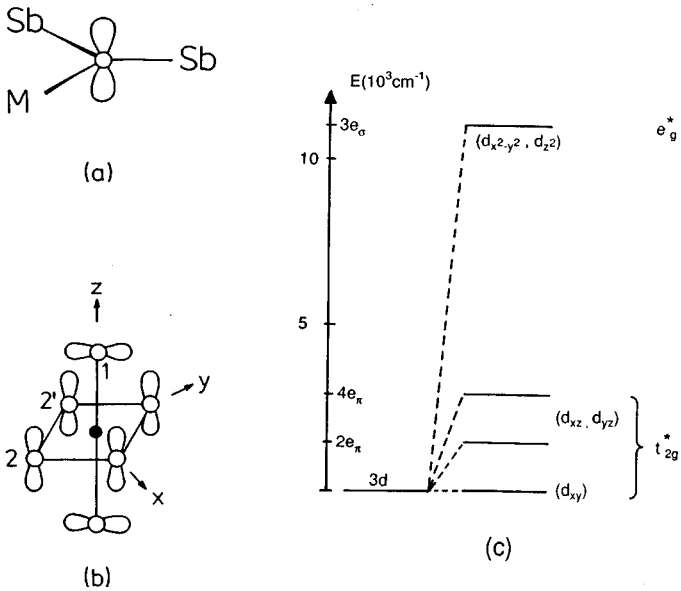

FIG. 9. The M–O bonding (d contributions) in the trirutile structure (MSb_2O_6)—the cationic coordination of the oxygen atoms (a), the oxygen orbitals with π-bonding ability (b), and the one-electron MO diagram for Cu^{2+} on the M position—assuming equal Cu–O spacings (204.7 pm) and neglecting the small angular distortion in the $Cu(O2)_4$ plane (c). Model calculation with $e_\sigma = 3675\ cm^{-1}$ and $e_\pi = 720\ cm^{-1}$. (b) also gives the molecular coordinate system for the CuO_6 polyhedra in $Zn_{1-x}Cu_xSb_2O_6$ mixed crystals (O2′ ≡ O2a, Table 3). In the case of compressed octahedra $g_\parallel$ and $g_\perp$ correlate with the z direction and the xy plane, respectively. For the elongated octahedra a correlation of $g'_\perp$ with the yz plane and of $g'_\parallel$ with the normal to this plane is consistent with the EPR results.

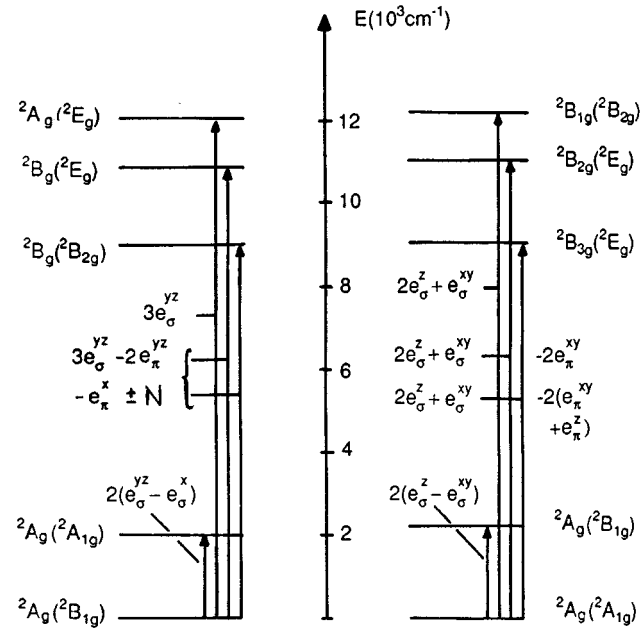

FIG. 10. Term diagram of Cu^{2+} in $ZnSb_2O_6$—compressed (right) and elongated (left) CuO_6 octahedra along the molecular z and x direction, respectively. The polyhedron symmetries are D_{2h} (compression) and C_{2h} (elongation), with the D_{4h} parent terms also given. The AOM energies refer to Cu–O spacings $a_z = 197$ pm, $a_{xy} = 208.5$ pm (compression) and $a_x = 212$ pm, $a_{yz} = 201$ pm (elongation). The AOM parameter set chosen for the averaged Cu–O distance (204.7 pm) is: $e_\sigma = 3675\ cm^{-1}$, $e_\pi = 720\ cm^{-1}$. The labeling of the AOM parameters (x, y, z) refers to the overlap of the metal d orbitals with the oxygen p orbitals in the respective molecular directions (Fig. 9). The nondiagonal energy N is $\{(e_\pi^{yz})^2 + (e_\pi^{yz} - e_\pi^{x})^2\}^{1/2}$ (see matrix in footnote 1).

$9600\ cm^{-1}$, if the center-of-gravity rule for the splittings of the octahedral E_g and T_{2g} parent levels is considered valid. This value is near that reported for Ni^{2+} in $NiSb_2O_6$ ($8900\ cm^{-1}$) (15), as expected for a $3d$ cation of the same charge, neighbored in the periodic table, and in an identical host structure with the same ligand atom. In rutile-type structures Δ (averaged octahedral value) equals $3e_\sigma - 2e_\pi$ (Fig. 9c), in difference to a situation where the π bonding is not restricted ($\Delta = 3e_\sigma - 4e_\pi$) (13,14).

The π anisotropy is also reflected by the covalency parameters $k_\perp$ (connected with the d_{xz}, d_{yz} MOs) for the compressed and $k'(d_{xy}), k'(d_{xz}, d_{yz})$ for the elongated CuO_6 octahedron (Eq. [4]). While the orbital reduction factors refering to d_{xz}, d_{yz} have values around 0.82(3), $k'(d_{xy})$ is much larger, $\cong 0.89$. The equations

$$k'(d_{yz}) \cong C\alpha\beta; \quad k'(d_{xz}) \cong C\alpha\gamma_1;$$
$$k'(d_{xy}) = C\alpha\gamma_2; \quad (C < 1)\ (13)) \qquad [7]$$

give approximate relations between the covalency factors $k \cong k'$, the mixing coefficient α in the ground state MO (Eqs. [1] and [3]) and the corresponding coefficients β and γ_1, γ_2 in the π-antibonding MOs originating from the d_{yz} and d_{xz}, d_{xy} orbitals, respectively. We roughly estimate that, because d_{xy} is expected to be nonbonding, $(\gamma_2 \approx 1) - \beta \approx \gamma_1$ is about 0.92. The latter approximate value nearly equals the α coefficient in the σ-antibonding d_z^2 ground state MO of the compressed octahedron (0.91) as derived from the hyperfine coupling. Both values are rather high for an oxidic solid and indicative of a preferentially ionic bond.

The Interplay of Host Site Strain and Vibronic Jahn–Teller Coupling

The octahedra in rutile-type structures are usually tetragonally compressed in the case that cations with closed-shell electron configurations occupy these positions. This host-site distortion is induced by packing effects and, possibly, by the π-bonding anisotropy discussed above. The Zn^{2+} octahedra in $ZnSb_2O_6$ are deformed according to $\rho \cong 4$ pm (Table 3). The extent of the distortion is enhanced to $\rho \cong 13$ pm by the Jahn–Teller effect, if Cu^{2+} replaces Zn^{2+} (or Mg^{2+}), yielding β-$CuSb_2O_6$.

$$\Delta E = 2A_1\rho_t \quad (\rho_t = \rho_m + \rho_s); \quad K_\varepsilon = A_1/\rho_m \qquad [8]$$

gives the relation between the first-order coupling constant A_1 and the ground state splitting ΔE (16). The latter is mainly caused by vibronic interactions of the Jahn–Teller type, but includes the host-site strain as well, with ρ_m and ρ_s refering to the Jahn–Teller and the strain distortion contribution, respectively. A_1 is calculated to be $\cong 85\ cm^{-1}\ pm^{-1}$, using the experimental radial distortion parameter for the CuO_6 polyhedron in β-$CuSb_2O_6$ ($\rho_t = 13$ pm) and the estimated ground state splitting of about 2200 cm^{-1} (Fig. 10). The magnitude of A_1 depends on the chosen overlap integrals and is enhanced (larger calculated ground state splitting) if S values for the charged Cu^{2+} ion are used. It is in the range expected for an oxidic solid though. The force constant of the involved Jahn–Teller active ε_g mode is $K_\varepsilon \cong 9.5\ cm^{-1}\ pm^{-2}$, applying the appropriate calculation formalism (16) (Eq. [8]). Here, $\rho_m \cong 9$ pm was used, because the host-site distortion contribution ($\rho \cong 4$ pm) can be considered as being vibronically silent. K_ε is extremely large, confirming that the restoring forces against a distortion are very strong, due to a stiff lattice.

The first-order Jahn–Teller coupling has no energetic preference for either an elongated or a compressed octahedral geometry. It is only the small higher order coupling terms which favor the elongation (4, 16). They are described by an angular distortion parameter φ, where $\varphi = 0°$, 120°, 240° correspond to octahedra elongated along z, x, and y, respectively, while $\varphi = 180°$, 300°, 60° indicate a compression along these molecular directions. The latter conformations correlate with the saddle points in the energy diagram of Fig. 11I, the former with the minima. The energy difference 2β between the extrema is typically about 5% of the ground state splitting in magnitude (17). A strain acting along the z direction, $\varphi = 180°$, will distort the ground state potential surface, reducing the saddle point energy at $\varphi = 180°$ and thus equally stabilizing two of the three minima. Eventually the zero-point vibronic level will be above the saddle point and will create a situation as that observed for $Zn_{1-x}Cu_xSb_2O_6$ mixed crystals with $x < 0.5$ (Fig. 11II). This vibronic state, centered at $\varphi = 180°$, is delocalized over a rather large $\delta\varphi$ range, which is expected to induce a $d_{x^2-y^2}$ contribution to the d_z^2 ground state and to increase the $g_\parallel$ value above g_0—as was indeed observed (vide supra).

Increasing the Cu^{2+} concentration to $x > 0.5$ apparently slightly enhances the higher order vibronic coupling constant due to cooperative elastic forces between the CuO_6 polyhedra,[3] thus creating a situation in which the lowest vibronic states are localized in the two lower minima (Fig. 11III). While usually the cooperative Jahn–Teller effect distinctly enhances the ground state splitting and the extent of the local distortion of the Cu^{2+} polyhedron, this is not so in this case—as clearly indicated by the d–d transition energies and the average g values (Table 4), which do not change with the Cu^{2+} concentration. Apparently only the interplay between the higher order coupling terms and the host site strain, which determine the warping structure (Fig. 11) of the ground state potential surface, is slightly, though significantly, influenced.

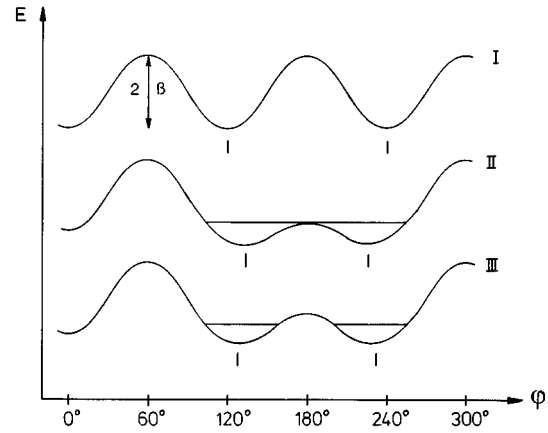

FIG. 11. Warping of the ground state potential surface of the CuO_6 polyhedra in mixed crystals $Zn_{1-x}Cu_xSb_2O_6$ by higher order vibronic coupling terms (2β) and the influence of a host-lattice strain (S) at $\varphi = 180°$—projection along the angular φ-coordinate: Situation (I) and (II; $x < 0.5$) without and with strain, respectively; III refers to mixed crystals with $x > 0.5$, where the 2β/S ratio is enhanced with respect to II.

The two lowest minima in Fig. 11III represent the two equivalent alternatives of an elongation, namely along the Cu–O(2a) or Cu–O(2) bond, corresponding to $\varphi \approx 120°$ and $\approx 240°$, respectively. The tendency to form twinned single crystals can be led back to the four possibilities of having the long axis along a Cu–O(2) (2a) bond in the two differently oriented CuO_6 polyhedra in the unit cell (Figs. 1 and 3). Thus the possibility to establish a long-range order of elongated CuO_6 octahedra corresponding to a strongly disturbed antiferrodistortive pattern ($2\gamma \approx 65°$) with increasing x is the presumable reason for switching from situation II to III (Fig. 11).

It should finally be mentioned that the positions of the two lower minima in the presence of strain (Figs 11II and 11III) are shifted from their original octahedral positions to $\varphi > 120°$ and $< 240°$, well in accord with the small distance anisotropy in the yz plane of the CuO_6 polyhedra in β-$CuSb_2O_6$ (Table 3).

The interplay between vibronic Jahn–Teller coupling of octahedral Cu^{2+} and host site strain has been studied in several cases, namely for mixed crystals $Ba_2Zn_{1-x}Cu_xF_6$ (17a) and $K_2Zn_{1-x}Cu_xF_4$ (17b) for example. In both systems

[3] Elastic coupling between neighbor CuL_6 polyhedra leads to a situation in which the preferred axes of elongation orient with respect to each other in a way that the unit cell distortion remains small. The directional correlation between different polyhedra generates cooperative order patterns of different symmetries, which may induce crystallographic phase transitions (4, 16).

also a transition from a local compressed to an elongated coordination occurs with increasing x. However, due to much more pronounced cooperative Jahn–Teller forces, which increase with increasing Cu^{2+} concentration, the local distortion becomes continuously larger. In the present case we meet the singular situation that the compressed-to-elongated transformation can be studied approximately without this additional parameter.

CONCLUSIONS

The presented results nicely demostrate that the energetically deciding factor for the ground state stabilization of the CuO_6 polyhedron is the linear Jahn–Teller coupling with no preference for any distortion geometry, so long as the distortion pathway corresponds to the octahedral ε_g mode. Only higher order vibronic coupling introduces a slight preference for the elongated geometry. If small strain effects of nearly the same magnitude as the higher order coupling terms are present, the geometry may switch from elongated to compressed. Interestingly enough, we can deduce from the spectroscopic results that clusters of elongated octahedra are present already at rather low Cu^{2+} concentrations. They are not ordered in a long-range pattern though, this occurring at a critical x value of 0.75 (295 K). The phase transition to the monoclinic structure is observed when the local distortion of the cooperatively ordered octahedra due to the Cu–O distance anisotropies in the xy planes cannot be cushioned by the tetragonal structure anymore.

The phase transitions of $CuSb_2O_6$ at 380 K can be understood as induced by a thermal averaging process between the two equivalent minima in Fig. 11III because vibronic states above the saddle-point are occupied at higher temperatures, leading to a fast dynamic exchange between the minima. This argument is supported by the crystallographic data. If the Cu–O(2) and Cu–O(2a) spacings thermally equilibrate, one obtains from the neutron diffraction data for β-$CuSb_2O_6$ (Table 1) $a_z = 200.4$ pm and $a_{xy} = 206.6$ pm—in rather good agreement with the X-ray single crystal data of 202.7 and 206.6 pm for the α phase. This "planar-dynamic" Jahn–Teller effect is expected to average the $g_2^{e'}$ and $g_3^{e'}$ values for the mixed crystals with $x > 0.5$ at higher temperatures, leading to $(g^{e'})_{\mathrm{dyn}}$. tensor components of $\cong 2.11_5$ and $\cong 2.28_5$. The EPR spectra of $CuSb_2O_6$, and those of the mixed crystals with high x values as well, are not in contradiction with this supposition, because the linewidth is so large at 295 K that a g-tensor anisotropy cannot be resolved anymore. Thus the β-to-α phase transition of $CuSb_2O_6$ appears to be of the order–disorder type, implying the change from a local elongated CuO_6 octahedron to a *dynamically averaged* compressed conformation (see Fig. 11III). In constrast, the CuO_6 polyhedra in Cu^{2+}-doped $Zn(Mg)Sb_2O_6$ are *statically* compressed, due to the rather strong host site strain influence (Fig. 11II). Here Cu–O spacings of 197 pm (a_z) and $208._5$ pm (a_{xy}) are estimated, with a much larger difference $a_{xy} - a_z$ ($\cong 11._5$ pm) than in the dynamic case ($\cong 6$ pm).

ACKNOWLEDGMENTS

We are grateful to Prof. Dr. M. Atanasov (Bulgarian Academy of Sciences, Sofia) for valuable discussions concerning the AOM treatment, Prof. Dr. H. Haeuseler for his assistance in the interpretation of the IR and Raman spectra, and Prof. Dr. B. L. Ramakrishna (Arizona State University, Tempe, AZ) for supplying spectroscopic and magnetic results on $CuSb_2O_6$ in the frame of a cooperation supported by NATO.

REFERENCES

1. A. Bystrom, B. Hock, and B. Mason, *Ark. Kemi Mineral. Geol. B* **15,** 1 (1941).
2. V. Propach and D. Reinen, *Z. Anorg. Allg. Chem.* **369**, 278 (1969).
3. A. Nakua, H. Yun, J. N. Reimers, J. E. Greedan, and C. V. Stager, *J. Solid State Chem.* **91,** 105 (1991).
4. D. Reinen and C. Friebel, *Struct. Bonding* (*Springer*) **37,** 1 (1979).
5. J. D. Donaldson, A. Kjekshus, D. G. Nicholson, and T. Ranke, *Acta Chem. Scand. Ser. A* **29,** 803 (1975).
6. E. J. Gabe, Y. Le Page, J. P. Charland, F. L. Lee, and P. S. White, *J. Appl. Crystallogr.* **22,** 384 (1989).
7. W. H. Bauer, *Z. Kristallogr.* **209,** 143 (1994).
8. R. Franck, C. Rocchiccioli-Deltcheff, and J. Guillermet, *Spectrochim. Acta A* **30,** 1 (1974).
9. E. Husson, Y. Repelin, and H. Brusset, *Spectrochim. Acta A* **35,** 1177 (1979).
10. A. Ozarowski and D. Reinen, *Inorg. Chem.* **24**, 3890 (1985). [See references therein].
11. A. M. Nakua and J. E. Greedan, *J. Solid State Chem.* **118,** 199 (1995).
12. D. Reinen and J. M. Dance, *in* "Inorg. Solid Fluorides" (P. Hagenmüller, Ed.), p. 525. Academic Press, San Diego, 1985.
13. C. K. Jørgensen, *Chem. Phys. Lett.* **1,** 11 (1967).
14. D. W. Smith, *Struct. Bonding* (*Springer*) **35,** 87 (1978); private communication.
15. D. Reinen, *Theoret. Chim. Acta* **5,** 312 (1966).
16. D. Reinen and M. Atanasov, *Magn. Resonance Rev.* **15,** 167 (1991).
17. (a) G. Steffen, D. Reinen, H. Stratemeier, M. J. Riley, M. A. Hitchman, M. Matthies, Recker, F. Wallrafen, and J. R. Niklas, *Inorg. Chem.* **29,** 2123 (1990); (b) D. Reinen and S. Krause, *Inorg. Chem.* **20,** 2750 (1981); M. J. Riley, M. A. Hitchman, and D. Reinen, *Chem. Phys.* **102,** 11 (1986).